PHYSICAL REVIEW B **84**, 064444 (2011)

Local electronic structure information contained in energy-filtered diffraction patterns

Ján Rusz,[1,2] Stefano Rubino,[3] Olle Eriksson,[1] Peter M. Oppeneer,[1] and Klaus Leifer[3]
[1]*Department of Physics and Astronomy, Uppsala University, Box 516, S-751 20 Uppsala, Sweden*
[2]*Institute of Physics, Czech Academy of Sciences, Na Slovance 2, CZ-182 21 Prague, Czech Republic*
[3]*Department of Engineering Sciences, Uppsala University, Box 534, S-751 21 Uppsala, Sweden*
(Received 24 June 2011; revised manuscript received 21 July 2011; published 30 August 2011)

We analyze the information contained in energy-filtered diffraction patterns measured on core-level edges. By inversion of the sum rules for electron energy loss near edge structures we calculate the reciprocal space distribution of the contribution to the total signal originating from spin moment, orbital moment, spin-orbital interaction, and individual components of magnetic and spin-orbital anisotropy tensors. We demonstrate, in particular, that the diffraction patterns contain information about all three vector components of the spin and orbital magnetic moments.

DOI: 10.1103/PhysRevB.84.064444 PACS number(s): 79.20.Uv, 75.30.−m, 68.37.Lp

I. INTRODUCTION

The quantitative understanding of orbital and spin magnetic moments on a microscopic level is key to many phenomena in modern magnetism. In this context, the x-ray magnetic circular dichroism (XMCD) technique is of central importance with its possibility to determine magnetic spin and orbital moments (m_S and m_L) in an atom-specific way. It was recently shown that the electron magnetic circular dichroism (EMCD) technique[1] in the transmission-electron microscope (TEM) can equally be used to determine the m_L/m_S ratio.[2] To determine the m_L/m_S ratio, both techniques, XMCD and EMCD, make use of sum rules.[3–6] In these, intensities measured in x-ray and electron-energy-loss spectra are related to the local magnetic characteristics. As was shown later, sum rules are not limited to spin and orbital moments. Also other physical properties described by a set of local operators discussed in Refs. 5 and 7 can be extracted from polarized spectral measurements. In the electron-energy-loss near-edge structures (ELNES)—the spectroscopic method behind the EMCD technique—the measured signal is a function of both electron energy loss and scattering vector $\mathbf{q}$. By inverting the sum rules expressions we develop an analysis tool, which allows one to study partial spectroscopic signals that originate from local magnetic characteristics described by each of these operators—as a function of scattering vector $\mathbf{q}$.

II. THEORY

Here we summarize the theory behind our calculations. A concise summary of the Bloch-waves theory is presented first, then the ELNES sum rules in rotationally invariant form are expressed in terms of irreducible operators introduced by Ankudinov and Rehr.[7] In the following section the sum rules are inverted in order to obtain simple algebraic expressions for real and imaginary parts of energy-integrated mixed dynamical form factors (MDFFs).

A. Bloch-waves approach

The Bloch-waves theory for calculation of the dynamical diffraction effects dates back to the middle of the last century[8] and entered textbooks about electron diffraction.[9,10] Its extension to electron-energy-loss spectroscopy was introduced independently by groups of Kohl and Schattschneider.[11,12] Here we will quote only the key expression, which will be helpful in the context of this work. We follow the notation of Ref. 13.

In a crystal, the double-differential scattering cross section (DDSCS) of fast electrons with energy E_0 and incoming wave vector $k_{\rm in}$ scattered into direction $k_{\rm out}$ and losing energy E is given by the expression

$$\frac{d^2\sigma}{d\Omega\, dE} = \frac{4\gamma^2}{a_0^2}\frac{k_{\rm out}}{k_{\rm in}}\sum_{\substack{jlj'l'\\ \mathbf{ghg'h'}}}\frac{1}{N_{\mathbf{a}}}\sum_{\mathbf{a}} X^{jlj'l'}_{\mathbf{ghg'h'}}(\mathbf{a})\frac{S_{\mathbf{a}}(\mathbf{q},\mathbf{q}',E)}{q^2 q'^2}, \quad (1)$$

where γ is the relativistic factor and a_0 is Bohr radius. Summation variables j,l,j',l' are indexing the Bloch waves—the eigenstates of fast electrons in a crystalline sample, $\mathbf{g},\mathbf{h},\mathbf{g}',\mathbf{h}'$ index their plane-wave components. Index $\mathbf{a}$ labels the atom positions in the sample and $N_{\mathbf{a}}$ is the number of these scattering centers. Vectors $\mathbf{q},\mathbf{q}'$ denote momentum transfers between the plane-wave components of the Bloch waves. Approximately, one can write $\mathbf{q} = \mathbf{k}_{\rm out} - \mathbf{k}_{\rm in} + \mathbf{h} - \mathbf{g}$ and similarly for $\mathbf{q}'$. More precisely, $\mathbf{q}$ also depends on indices j and l (see Ref. 13 for more details). The matrix element $S_{\mathbf{a}}(\mathbf{q},\mathbf{q}',E)$ is the energy-loss-dependent MDFF,[14] which will be the subject of the following sections. Finally, the coefficient $X^{jlj'l'}_{\mathbf{ghg'h'}}(\mathbf{a})$ is a shorthand notation for a product of Bloch coefficients and phase factors (see Ref. 13).

A remark on the notation: In the expression above we used $S(\mathbf{q},\mathbf{q}',E)$ to denote the energy-dependent MDFF. The sum rules are expressed via energy integrals of spectra over an energy range of a selected core level (edge). Because the energy dependence of DDSCS is mainly determined by the MDFFs, it will be useful to introduce a notation for energy-integrated MDFFs over a particular edge $j\pm$ (where $j\pm \equiv l \pm s$; l and s are orbital and spin magnetic moments of the initial states, respectively). We will use $S_{j\pm}(\mathbf{q},\mathbf{q}')$ to denote the MDFF integrated over the energy region corresponding to the $j\pm$ edge, i.e., dropping the energy variable E and attaching the edge index $j\pm$. In a somewhat unfortunate clash of notation, the "S" will be used also as a spin operator, but always with the "hat" sign, e.g., $\hat{\mathbf{S}}$ or $\hat{S}_i$ for a vector spin operator or its Cartesian component ($i = x,y,z$).

B. ELNES sum rules

Ankudinov and Rehr[7] presented a complete set of six dipole sum rules for the x-ray absorption spectroscopy (XAS) spectra, which can be expressed in terms of the following six operators:

$$\hat{O}_1 = 2L(2L-1)N_h\hat{1}/(3N_e), \tag{2}$$

$$\hat{O}_{2;i} = (2L-1)\hat{L}_i, \tag{3}$$

$$\hat{O}_{3;ij} = (\hat{L}_i\hat{L}_j + \hat{L}_j\hat{L}_i)/2 - \delta_{ij}L(L+1)\hat{1}/3, \tag{4}$$

$$\hat{O}_{4;i} = 2L(L-1)[\hat{S}_i - (\hat{L}_i\hat{\mathbf{L}}\cdot\hat{\mathbf{S}} + \hat{\mathbf{L}}\cdot\hat{\mathbf{S}}\hat{L}_i)/L], \tag{5}$$

$$\hat{O}_5 = 2(L-1)\hat{\mathbf{L}}\cdot\hat{\mathbf{S}}/L, \tag{6}$$

$$\hat{O}_{6;ij} = \hat{L}_i(\hat{\mathbf{L}}\cdot\hat{\mathbf{S}})\hat{L}_j + \hat{L}_j(\hat{\mathbf{L}}\cdot\hat{\mathbf{S}})\hat{L}_i - L(\hat{L}_i\hat{S}_j + \hat{L}_j\hat{S}_i), \tag{7}$$

where i,j are coordinate components and L is an orbital quantum number of final states in dipole transitions from initial states with an orbital quantum number l. We assume $l \to l+1 \equiv L$, i.e., we neglect the $l \to l-1$ transitions. N_h and N_e denote the number of holes and number of electrons, respectively, in the shell with orbital quantum number L. These are connected by the relation $N_h = 2(2L+1) - N_e$. $\hat{\mathbf{S}}$ and $\hat{\mathbf{L}}$ are spin and orbital momentum vector operators; $\hat{1}$ is the unity operator, i.e., $\mathrm{Tr}[\hat{1}\hat{\rho}_L] = N_e$ with $\hat{\rho}_L$ a density matrix—all operators acting within the dipole-selected shell of final states.

As shown in Ref. 7, it is possible to express an integrated XAS spectrum as a linear combination of ground-state mean values of $\hat{O}_1,\ldots,\hat{O}_6$ operators multiplied by photon polarization vectors. Or vice versa, suitable linear combinations of polarized XAS spectra allow one to separate a mean value of any of these six operators. This is one of the ways to derive the well-known spin and orbital moment XMCD sum rules.[3,4]

A useful relation between the operator $\hat{O}_4$ and the magnetic dipole moment operator $\hat{\mathbf{T}}$ allows one to reformulate Eq. (5) into a more familiar, but equivalent form,

$$\hat{O}_{4;i} = \frac{2}{3}(2L-1)L(L-1)\left[\hat{S}_i + \frac{2L+3}{L}\hat{T}_i\right]. \tag{8}$$

Contrary to x-ray absorption, the EELS spectra cannot be described by a single inelastic transition matrix element with well-specified momentum-transfer vectors. The EELS spectrum is a combination of a multitude of inelastic transition with various momentum-transfer vectors $\mathbf{q},\mathbf{q}'$ weighted by coefficients given by dynamical diffraction conditions. This had to be taken into account in the derivation of the EELS sum rules. The spin and orbital EMCD sum rules have been independently reported in two articles by Calmels *et al.*[6] and Rusz *et al.*[5] The latter work presents a complete set of four electron-energy-loss spectroscopy (EELS) dipole transition sum rules in a rotationally invariant form, which we will briefly show below.

To derive the final expressions for the EELS sum rules we need to find an equivalent of a difference spectrum as in XMCD. For that we need two different final wave-vector directions $\mathbf{k}_{\mathrm{out}}$, which are connected by a symmetry operation of the whole experimental geometry, including incoming beam and crystal structure orientation. Particularly, we need a symmetry operation that inverts the direction of magnetic moments, such as a mirror plane parallel to magnetic-moment directions. In such conditions it can be shown that the two measured spectra can be simulated with the same Bloch fields; just the order of vectors $\mathbf{q},\mathbf{q}'$ in MDFFs becomes interchanged, which, in turn, inverts the sign of the imaginary part of the MDFF. Assuming that we can identify two such wave vectors $\mathbf{k}_{\mathrm{out1}}$ and $\mathbf{k}_{\mathrm{out2}}$, we denote the sum and difference of corresponding spectra by $S(E)$ and $D(E)$, and their energy integrals over a particular edge j we denote simply as S_j and D_j. Then the complete set of ELNES sum rules can be formulated in the following form:

$$D_{j+} + D_{j-} = \sum_{\mathbf{q}\mathbf{q}'} K_{\mathbf{q}\mathbf{q}'}(\mathbf{q}\times\mathbf{q}')\frac{\langle\hat{O}_2\rangle}{2}, \tag{9}$$

$$\frac{D_{j+}}{L} - \frac{D_{j-}}{L-1} = \sum_{\mathbf{q}\mathbf{q}'} K_{\mathbf{q}\mathbf{q}'}(\mathbf{q}\times\mathbf{q}')\frac{\langle\hat{O}_4\rangle}{2L(L-1)}, \tag{10}$$

$$S_{j+} + S_{j-} = \sum_{\mathbf{q}\mathbf{q}'} K_{\mathbf{q}\mathbf{q}'}\mathbf{q}\cdot\left[N_e\langle\hat{O}_1\rangle + \langle\hat{O}_3\rangle\right]\cdot\mathbf{q}', \tag{11}$$

$$\frac{S_{j-}}{L-1} - \frac{S_{j+}}{L} = \sum_{\mathbf{q}\mathbf{q}'} K_{\mathbf{q}\mathbf{q}'}\mathbf{q}\cdot[L^2\langle\hat{O}_5\rangle + \langle\hat{O}_6\rangle]\cdot\mathbf{q}', \tag{12}$$

where the coefficient $K_{\mathbf{q}\mathbf{q}'}$ summarizes all prefactors, including the multiple product of Bloch coefficients and atom-dependent phase factors $X^{jlj'l'}_{\mathbf{ghg'h'}}(\mathbf{a})$, originating from dynamical diffraction effects, i.e.,

$$K_{\mathbf{q}\mathbf{q}'} = \frac{4\gamma^2}{a_0^2}\frac{k_{\mathrm{out}}}{k_{\mathrm{in}}}\frac{1}{N_{\mathbf{a}}}\sum_{\mathbf{a}}\sum_{\substack{\mathbf{gh}jl\to\mathbf{q}\\ \mathbf{g'h'}j'l'\to\mathbf{q}'}} X^{jlj'l'}_{\mathbf{ghg'h'}}(\mathbf{a})\frac{M_L(q,q')}{q^2q'^2} \tag{13}$$

[see Eq. (1)]. For more details we refer the reader to Refs. 5 and 13.

C. Inversion of sum rules

The procedure of deriving the EELS sum rules can be inverted: i.e., we can express an energy-integrated MDFF in terms of mean values of operators $\hat{O}_1\cdots\hat{O}_6$. It is a relatively lengthy, but straightforward procedure, and we will state only the final expressions,

$$\mathrm{Re}[S_{j\pm}(\mathbf{q},\mathbf{q}')] \propto \frac{L-\delta_{j-}}{2L-1}\langle\hat{X}\rangle \pm \frac{L(L-1)}{2L-1}\langle\hat{Y}\rangle, \tag{14}$$

$$\mathrm{Im}[S_{j\pm}(\mathbf{q},\mathbf{q}')] \propto \frac{(\mathbf{q}\times\mathbf{q}')}{2(2L-1)}[(L-\delta_{j-})\langle\hat{O}_2\rangle \pm \langle\hat{O}_4\rangle], \tag{15}$$

where

$$\hat{X} = (\mathbf{q}\cdot\mathbf{q}')N_e\hat{O}_1 + \mathbf{q}\cdot\hat{O}_3\cdot\mathbf{q}', \tag{16}$$

$$\hat{Y} = -(\hat{\mathbf{q}}\cdot\hat{\mathbf{q}}')L^2\hat{O}_5 + \mathbf{q}\cdot\hat{O}_6\cdot\mathbf{q}'\mathbf{s}. \tag{17}$$

Combining these expressions with Eqs. (1) and (13) we can calculate the diffraction pattern integrated over a selected edge j by equation

$$\left.\frac{d\sigma}{d\Omega}\right|_j \equiv \frac{1}{2}(S_j + D_j) \propto \sum_{\mathbf{q}\mathbf{q}'} K_{\mathbf{q}\mathbf{q}'}S_j(\mathbf{q},\mathbf{q}'). \tag{18}$$

TABLE I. *Ab initio* calculated mean values of operators present in the model expressions for energy-integrated MDFF for $L_{2,3}$ edges ($L = 2$) of late $3d$ transition metals. All values are calculated in local density approximation within an atomic sphere with a radius of 2.3 Bohr radii using the WIEN2k code,[15] assuming magnetization orientation along the (001) direction.

	bcc Fe	hcp Co	fcc Ni
N_h	3.904	2.837	1.761
$\|\|\langle\hat{\mathbf{L}}\rangle\|\|$	0.048	0.086	0.049
$\|\|\langle\hat{\mathbf{S}}\rangle\|\|$	1.130	0.842	0.329
$\|\|\langle\hat{\mathbf{T}}\rangle\|\|$	2.8×10^{-4}	9.6×10^{-4}	2.0×10^{-4}
$\langle\hat{\mathbf{L}} \cdot \hat{\mathbf{S}}\rangle$	−0.051	−0.062	−0.049

Now we have a powerful tool to calculate how a signal originating solely from, let us say, the x component of the orbital magnetic momentum is distributed in the diffraction plane. For this case (assuming the total orbital moment to be normalized to one) we simply put in Eqs. (14)–(17) the $\langle\hat{L}_x\rangle \equiv 1 \longrightarrow \langle\hat{O}_{2;x}\rangle = (2L - 1)$ and set mean values of the y and z componets of this operator (as well as all the other operators) to zero and calculate the diffraction pattern using Eq. (18). Such calculations are reported in the next section.

Note a useful secondary outcome of these formulas: We have obtained expressions for an *ab initio* dipole approximation of energy-integrated MDFFs, since all the mean values present in these expressions can be easily evaluated by electronic structure calculations. As an example, we show such values for bcc iron, hcp cobalt, and fcc nickel in Table I, assuming that the anisotropy operators have negligible mean values.

Accuracy of the dipole approximation for MDFF was discussed in Ref. 13. It is known that for larger momentum-transfer vectors, dipole approximation overestimates the MDFF, which could reduce the accuracy of simulations at larger scattering angles. In the above-mentioned manuscript it was shown that so-called $\lambda = 1$ approximation improves accuracy significantly. That can be added to Eqs. (14) and (15) by explicitly including the radial integral $M_L(q, q')$ from Eq. (13), expressed via spherical Bessel functions instead of their linear approximations. Note that such extension also requires a knowledge of radial parts of initial- and final-state wave functions. Nevertheless, in the following text, we use a simple dipole approximation in which $M_L(q,q')$ is q,q' independent.

III. RESULTS AND DISCUSSION

Here we summarize the results of our calculations for various experimental geometries. The signal maps originating from various operators are presented and their symmetries are analyzed.

We chose the following parameters for our calculations: The assumed crystal structure is body-centered cubic with lattice parameters of bcc iron. The crystal surfaces are parallel, with normals along the (001) direction. Acceleration voltage was set to 300 keV. In systematic row calculations we assumed a beam tilt toward the (016) direction, i.e., approximately 10° tilt from (001) zone-axis orientation. This means that the systematic row reflections are multiples of $\mathbf{G} = (200)$. All diffraction patterns are calculated on a grid of $4.6G_{(200)} \times 4.6G_{(200)}$ with step $0.05G_{(200)}$, with center at the transmitted beam and q_x axis along the systematic row with multiples of $\mathbf{G}_{(200)}$.

The Cartesian coordinates x, y, z are oriented according to the lattice vectors $\mathbf{a}, \mathbf{b}, \mathbf{c}$. The lattice vector $\mathbf{c}$ is parallel to the sample surface normals.

The dynamical diffraction calculations were performed using the program DYNDIF, first reported in Ref. 13, with the improved Bloch-waves convergence scheme.[16] The convergence parameter was set to 10^{-5}, providing highly converged results.

First we will state some general results originating from symmetry and algebraic structure MDFF expressions. In total, the operators $\hat{O}_1 \cdots \hat{O}_6$ have 26 components, since we have two scalar operators ($\hat{O}_1$ number of particles and $\hat{O}_5$ spin-orbital interaction), two vector operators ($\hat{O}_2$ orbital moment and $\hat{O}_4$ spin moment + magnetic dipole term), and two tensor operators describing anisotropies. However, several of those will lead to the same signal distribution in the diffraction plane, up to an edge-dependent constant factor.[17] For example, the spin-orbital interaction will give the same signal distribution as the number of holes, or the x component of orbital momentum will have the same signal distribution as the x component of spin momentum. They will only differ by an edge-dependent prefactor. Another reduction of the number of different distributions comes from the symmetry of the tensors $\hat{O}_4$ and $\hat{O}_6$ stating $\hat{O}_{ij} = \hat{O}_{ji}$. Taking this into account, there can be only ten different signal distributions, namely, one from a scalar operator (let us choose N_h, number of holes), three from a vector operator (e.g., spin moment vector components), and three diagonal and three off-diagonal tensor components (e.g., anisotropic spin-orbit tensor $\hat{O}_6$). We have calculated all these distributions separately by always setting one of these ten components to 1 and all the others to zero.

A. Two-beam case

We will show results first for the two-beam geometry, which was the first suggested geometry for observation of the EMCD signal.[18] The incoming beam direction is set to (016). The thickness-dependent maps of the signals from all ten independent components are shown in Fig. 1.

By far the strongest relative signal comes from scalar operators, i.e., number of holes N_h and also spin-orbital interaction $\langle\hat{O}_5\rangle$ (not shown). A reciprocal space distribution of these signals is shown in the first column of Fig. 1. This contribution essentially determines the shape of the observed diffraction pattern, including the thickness-dependent Pendellösung oscillations of the intensities of the transmitted beam and the Bragg-diffracted beam $\mathbf{G} = (200)$.

In practice, for lighter elements the value of N_h is larger than the mean value of spin-orbital interaction $\langle\hat{O}_5\rangle$, therefore it is the $\langle\hat{O}_1\rangle \propto N_h$ that is the major contribution. For spin-orbit split edges, such as L_3 and L_2, one can see from the first term of Eq. (14) that N_h contributions are scaled in ratio 2 : 1 (or L vs $L - 1$, in general). The spin-orbital interaction in the valence band then distorts this ratio by adding contributions of opposite signs to L_2 vs L_3 intensities, according to the second term of Eq. (14). For instance, at the $M_{4,5}$ edges of

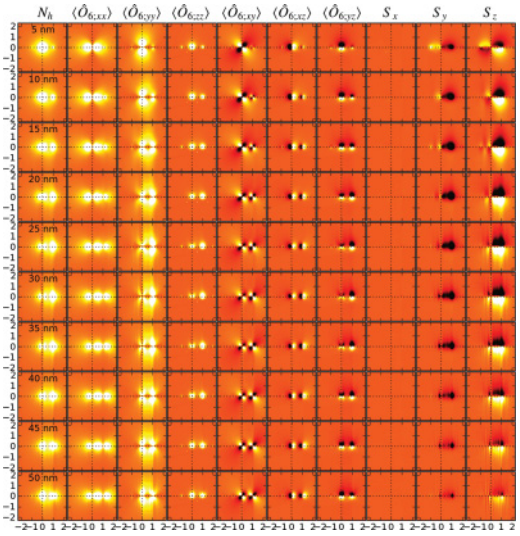

FIG. 1. (Color online) Reciprocal space distribution of the signal, Eq. (18), at the L_3 edge from number of holes, spin-orbital anisotropic tensor (xx,yy,zz,xy,xz,yz), and spin moment vector (x,y,z) components for two-beam case geometry. The signal from the number of holes is scaled down by a factor of 20. The vertical and horizontal axes give q_x and q_y in multiples of $G_{(200)}$.

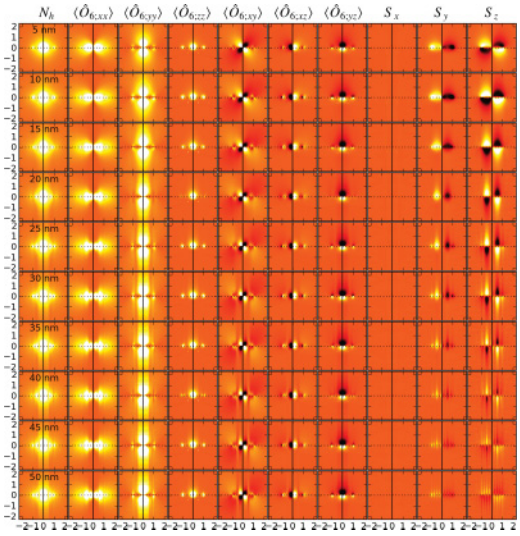

FIG. 2. (Color online) The same as in Fig. 1, but for the three-beam geometry.

actinides, the ratio of signal strength deviates considerably from 3 : 2 (Ref. 19) due to strong spin-orbital interaction in the valence $5f$ states. If we can neglect (or remove) other contributions rather than N_h and spin-orbital interaction, we can separate out the N_h and spin-orbit contributions owing to the difference of their prefactors for L_3 vs L_2 edge. This is actually used in the formulation of the "N" and "spin-orbit" sum rules in the XAS.[7,19] Similarly we separate the orbital moment contribution from the spin moment (plus the magnetic dipole term).

The signal from diagonal elements of the anisotropy tensors $\langle\hat{O}_3\rangle$ and $\langle\hat{O}_6\rangle$ has an interesting distribution. The zz component more or less enhances the Bragg spots, although one can observe its tendency to shift the maxima toward the positive q_y direction. That seems to be a consequence of the tilt, as will be seen below. The xx and yy components are stronger. The xx component has a tendency to add a signal in between the spots on the systematic row, forming a dumbbell-like structure along the systematic row. The yy component similarly adds a signal aside the spots, but in this case in the perpendicular direction to the systematic row. All these diagonal components lead to solely positive contributions to the diffraction pattern.

The signal from off-diagonal elements of the anisotropy tensors has varying sign throughout the diffraction plane. The xy component forms d-orbital-like shapes, four-leaf clovers, which are centered on Bragg spots. Their intensity follows the Pendellösung oscillations. In case of a strong contribution from this term, the Bragg spots would be slightly deformed into elliptic shapes with diagonal main axes. The xy and yz components lead to a displacement of the Bragg spot positions along q_x and q_y directions, respectively.

Note that in cubic crystals the anisotropy contributions should vanish, unless there is a spontaneous breaking of symmetry, for example, an orbital ordering observed in manganites.[20] In other words, observation of anisotropy signal in diffraction patterns can be used to study changes of the local symmetry under phase transitions, even when the crystal structure stays the same.

The magnetic contributions, which are the core of the EMCD phenomenon, are shown in the last three columns. According to a simplified interpretation of EMCD, stressing its analogies with XMCD,[1] one would expect to observe only a signal from the magnetization parallel to the beam direction. We can see here that, in general, this is not the case. This will be seen more clearly in the zone-axis calculations below. However, already here we can see that there is clearly a signal from both S_y and S_z components and that they are all different from each other[21] (note that S_y has a signal *on the systematic row*). This means that the EMCD experiment is sensitive to both in-plane and out-of-plane magnetization components. A more detailed discussion of distribution of the magnetic signal is found in the next section, since the three-beam setup is the preferred geometry for quantitative EMCD measurements.[2,22]

B. Three-beam case

The three-beam geometry was shown to be a preferred choice for EMCD measurements due to its higher symmetry and possibility to use signals from all four quadrants of the diffraction plane by means of a *double difference* method.[2,16] An inspection of the nonmagnetic contributions to the diffraction pattern shows that all observations made in the previous section also apply here. The only additional property of maps in Fig. 2 is a symmetry or antisymmetry of contributions with respect to a vertical mirror axis passing through the transmitted beam. This gives us the possibility to exploit symmetries to enhance or remove certain contributions from the diffraction plane by adding or subtracting the two diffraction half-planes from each other.

Here we will mainly focus on the distribution of the magnetic signal in the diffraction plane. Similarly to the two-beam geometry, a magnetization along the x direction does not produce a visible signal,[23] which is a consequence

of the dynamical diffraction. Qualitatively we can argue in the following way: Eq. (15) shows that the magnetic-moment components are scalarly multiplied by $\mathbf{q} \times \mathbf{q}'$. We can estimate typical relative sizes of x, y, z components of this vector product. There are numerous contributions with large momentum transfer along the systematic row (i.e., the x direction), where all the strongly excited Bragg spots are located. For the y direction, q_y components will mainly originate from placement of the detector relative to the incoming beam and eventually from excited spots outside the systematic row of reflections. Finally, for the z direction, apart from weak Bragg spots outside the systematic row, the main source of q_z is only the energy-loss process that shortens the beam wave vector. Therefore the magnetization components, which contain the prefactor q_x, will produce much stronger signals than the others. Therefore the x component of $\mathbf{q} \times \mathbf{q}'$ is on average much smaller than y and z components, which explains why the x component of the magnetization is suppressed in the systematic row geometry.

Thus, the signal originating from the x component of magnetization is weak, and conversely, contributions from y- and z-direction magnetizations are much larger and mutually of similar magnitude. Both have the same symmetry, therefore in the three-beam geometry we cannot easily separate them. Nevertheless, we have demonstrated that experiments measuring EMCD in Lorentz mode should be able to detect in-plane magnetization in magnetic thin films.[24]

Note that the signal originating from magnetization in the y direction provides a nonzero signal directly at Bragg spots (200) and ($\bar{2}00$). Due to the antisymmetry of the magnetic signal with respect to the vertical mirror plane, this component has opposite sign at (200) and ($\bar{2}00$) spots. The presence of such signal components introduces a difference of the total intensities of the {200} spots, despite that we are in an exact three-beam orientation—i.e., expecting their intensities to be the same. Relative strength of this effect is thickness dependent. In our chosen geometry the signal per unit of magnetic moment reaches more than 5% of the signal per hole under 10 nm and about 3% at 20 nm, respectively. Therefore it should be feasible to detect in-plane magnetization via measurement of the difference of intensities of crystallographically equivalent Bragg spots. As an additional check one can use the fact that on spin-orbit split edges, such as L_3 and L_2, the asymmetry of intensities switches sign.

C. Zone-axis conditions

The zone-axis geometry is the most symmetric geometry setup. Though, at first sight it seems to be rather challenging for EMCD measurements due to strong dynamical diffraction effects, which sensitively alter the distribution of the magnetic signal as a function of thickness and orientation.[16] Nevertheless, the zone-axis geometry allows one to observe the EMCD signal and if the experimental conditions can be precisely set and kept stable during the measurement of energy-filtered TEM data cubes,[2,22] it would provide substantial advantages compared to systematic row geometries.

Most of the observations about properties of nonmagnetic contributions made in previous sections apply here as well. Of course, we now have higher symmetry, which makes all diagonal components of anisotropic tensors symmetric with respect to both horizontal and vertical mirror axes (Fig. 3). The xx and yy components bring certain rectangular distortions, while the zz component seems to only enhance the Bragg spots. The xy component forms four-leaf clover shapes, and xz and yx form dumbbell shapes along the x and y directions, respectively, at the positions of Bragg spots.

Due to increased symmetry in the zone-axis orientation, the operator maps for magnetization directions x and y differ only by a rotation of 90° (similarly for $\langle \hat{O}_{6;xx} \rangle$ vs $\langle \hat{O}_{6;yy} \rangle$ and $\langle \hat{O}_{6;xz} \rangle$ vs $\langle \hat{O}_{6;yz} \rangle$, respectively). This is of course expected, because from the dynamical diffraction point of view the q_x and q_y directions are symmetrically equivalent and the local electronic structure with magnetization along the x direction is equivalent to magnetization along the y direction after rotating by 90°.

In Ref. 24 it was observed that the signal from in-plane magnetization depends on the energy loss. We have studied this influence in the zone-axis orientation by artificially changing the energy-loss value. By reducing the energy-loss value the in-plane magnetization signal becomes weaker. This can be qualitatively explained in the following way. In order to observe, let us say, magnetization along the x direction, the momentum-transfer cross products $\mathbf{q} \times \mathbf{q}'$ must have a nonzero x component [see Eq. (15)]. That requires nonzero q_z components of momentum-transfer vectors. There are three sources of the nonzero q_z in the scattering processes: (1) shift of detector orientation, which tilts the k_{out}, (2) energy loss, which shortens the k_{out}, and (3) contributions from higher-order Laue zones. The first effect increases linearly with the square root of the acceleration voltage and quadratically as a function of scattering angle, $q_z = k_f(1 - \cos\,\Theta) \propto \sqrt{U}\Theta^2$, where U is the acceleration voltage and Θ is the scattering angle. The value of q_z reaches 0.05 a.u.$^{-1}$ at 25 mrad scattering angle and 300 keV acceleration voltage. Compared to typical reciprocal lattice cell sizes, e.g., $a^\star = 1.16$ a.u.$^{-1}$ for bcc iron, it is a very weak effect. The second effect provides $\frac{q_z}{k_f} = 1 - \frac{k_f}{k_i} = 1 - \sqrt{\frac{U}{U-E}} \approx -\frac{E}{2U}$, where E is the energy loss. At 300 kV voltage and an energy loss of 700 eV it gives $q_z \approx 0.2$ a.u.$^{-1}$, which is a considerably stronger effect. It is not easy to qualitatively evaluate the contribution from higher Laue zones, because that strongly depends on the dynamical diffraction effects. However, when we artificially set the energy loss to zero, the signal from in-plane magnetization dropped down approximately by factors of 5–10, which suggests that higher-order Laue-zone excitations do not contribute stronger than tilting the k_{out}. We can conclude that the intensity of the in-plane magnetization signal scales approximately linearly with the energy loss. For energy losses below 100 eV it becomes a rather weak effect.

It is interesting to note that in an exact (001) zone-axis orientation of a cubic crystal, we can separate contributions from all three components of the magnetization vector from a single diffraction pattern (Fig. 3). Observe that the signal from the x component is symmetric with respect to the k_y axis, while both y and z components lead to an antisymmetric distribution of the signal with respect to that axis. Therefore if we sum the left diffraction half-plane with a mirror image of the right diffraction half-plane, we remove contributions from the

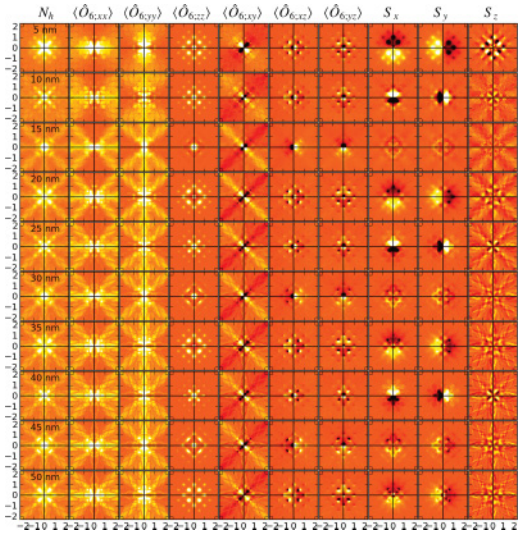

FIG. 3. (Color online) The same as in Fig. 1, but for (001) zone-axis geometry.

y and z components, while the x contribution becomes doubled. A subsequent difference of the upper and lower diffraction quarter-planes removes the contributions from the N term and spin-orbit term. It also removes the eventual contributions from tensor operators $\hat{O}_3$ and $\hat{O}_6$, with the exception of their yz term, the contribution of which has the same symmetry properties as the contribution from the x component of the magnetic signal. In an analogous way we can extract the signal from the y component of the magnetization.

The contribution from the z component of the magnetization is antisymmetric to both horizontal and vertical mirror axes, therefore it can be extracted by the double difference procedure.[2] Its antisymmetry with respect to the $k_x = k_y$ line can moreover be used to remove the eventual xy components from the anisotropy tensors.

Thus a single measurement of a diffraction pattern in the zone-axis orientation allows one, in principle, to probe the magnetization vector in all three dimensions and that is a unique feature of EMCD. It is necessary to say, though, that such analysis is only possible for structures with sufficiently high symmetry, otherwise there might not be a sufficient number of symmetry operations, which would allow such simple separation.

IV. CONCLUSIONS

We have analyzed the physical information contained in energy-filtered diffraction patterns. In the dipole approximation the signal is composed of distributions originating from the number of holes, spin-orbital interaction, spin and orbital magnetic moments, and anisotropy tensors. In the case of highly symmetric diffraction patterns it is possible to isolate individual components by exploiting its symmetry properties. In more general cases, one can use such maps to fit the measured diffraction pattern in order to decompose it into a combination of theoretical distributions from individual components of $\hat{O}_1, \ldots, \hat{O}_6$, in a way similar to that used in Refs. 25 and 26.

We have shown that such diffraction patterns contain information about all three components of the magnetization vector—a unique feature of EMCD compared to x-ray-based techniques.

As a side result, we have formulated an *ab initio*-based dipole approximation for calculating mixed-dynamic form factors. It allows for efficient evaluation of energy-integrated MDFFs over a particular edge as a function of a few physical properties, which are easily obtainable from electronic structure calculations.

We note that the formalism in the present paper can be generalized beyond the dipole approximation by using methods described in Ref. 27 to study higher multipole terms,[28] such as quadrupoles, octupoles, or even the exotic rank five triacontadipole term suggested to be responsible for hidden order in URu_2Si_2.[29]

ACKNOWLEDGMENTS

This research was supported by Swedish Research Council and STINT. O.E. acknowledges financial support from ERC and the Knut and Alice Wallenberg Foundation. The simulations were performed on resources provided by the Swedish National Infrastructure for Computing (SNIC).

[1] P. Schattschneider, S. Rubino, C. Hébert, J. Rusz, J. Kuneš, P. Novák, E. Carlino, M. Fabrizioli, G. Panaccione, and G. Rossi, Nature **441**, 486 (2006).

[2] H. Lidbaum, J. Rusz, A. Liebig, B. Hjörvarsson, P. M. Oppeneer, E. Coronel, O. Eriksson, and K. Leifer, Phys. Rev. Lett. **102**, 037201 (2009).

[3] B. T. Thole, P. Carra, F. Sette, and G. van der Laan, Phys. Rev. Lett. **68**, 1943 (1992).

[4] P. Carra, B. T. Thole, M. Altarelli, and X. Wang, Phys. Rev. Lett. **70**, 694 (1993).

[5] J. Rusz, O. Eriksson, P. Novák, and P. M. Oppeneer, Phys. Rev. B **76**, 060408(R) (2007).

[6] L. Calmels, F. Houdellier, B. Warot-Fonrose, C. Gatel, M. J. Hÿtch, V. Serin, E. Snoeck, and P. Schattschneider, Phys. Rev. B **76**, 060409(R) (2007).

[7] A. Ankudinov and J. J. Rehr, Phys. Rev. B **51**, 1282 (1995).

[8] Y. Kainuma, Acta. Crystallogr. **8**, 247 (1955).

[9] D. B. Williams and C. B. Carter, *Transmission Electron Microscopy* (Springer, New York, 2009).

[10] R. F. Egerton, *Electron Energy-Loss Spectroscopy in the Electron Microscope*, 2nd ed. (Plenum, New York, 1996).

[11] A. Weickenmeier and H. Kohl, Philos. Mag. B **60**, 467 (1989).

[12] M. Nelhiebel, P.-H. Louf, P. Schattschneider, P. Blaha, K. Schwarz, and B. Jouffrey, Phys. Rev. B **59**, 12807 (1999).

[13] J. Rusz, S. Rubino, and P. Schattschneider, Phys. Rev. B **75**, 214425 (2007).

[14] H. Kohl and H. Rose, Adv. Electron. Electron Phys. **65**, 173 (1985).

[15]P. Blaha, K. Schwarz, G. K. H. Madsen, D. Kvasnicka, and J. Luitz, WIEN2k, An Augmented Plane Wave Plus Local Orbitals Program for Calculating Crystal Properties (Karlheinz Schwarz, Techn. Universität Wien, Austria, 2001).

[16]J. Rusz, e-print arXiv:0910.3849v1.

[17]This edge dependence typically allows one to separate them out, if measurements at both edges are available (e.g., both L_2 and L_3, or M_4 and M_5, etc.).

[18]C. Hébert and P. Schattschneider, Ultramicroscopy **96**, 463 (2003).

[19]K. Moore and G. van der Laan, Rev. Mod. Phys. **81**, 235 (2009).

[20]T. Hotta and E. Dagotto, Physica B **312–313**, 700 (2002).

[21]More precisely, they are linearly independent, i.e., no linear combination of these two will give zero in the whole diffraction plane.

[22]B. Warot-Fonrose, C. Gatel, L. Calmels, V. Serin, and P. Schattschneider, Ultramicroscopy **110**, 1033 (2010).

[23]The signal from magnetization along the systematic row is two orders of magnitude weaker than the signal from magnetization in other directions.

[24]S. Rubino, P. Schattschneider, J. Rusz, J. Verbeeck, and K. Leifer, J. Phys. D: Appl. Phys. **43**, 474005 (2010).

[25]C. Witte, N. J. Zaluzec, and L. J. Allen, Ultramicroscopy **110**, 1390 (2010).

[26]The calculated maps will readily serve as distribution maps of their corresponding spectral components—a straightforward generalization of the approach from Ref. 25 from one to two dimensions in the **q** space. Energy integrals of these spectral components are then in turn proportional to the mean values of their corresponding operators.

[27]G. van der Laan, Phys. Rev. B **57**, 5250 (1998).

[28]P. Santini, S. Carretta, G. Amoretti, R. Caciuffo, N. Magnani, and G. H. Lander, Rev. Mod. Phys. **81**, 807 (2009).

[29]F. Cricchio, F. Bultmark, O. Grånäs, and L. Nordström, Phys. Rev. Lett. **103**, 107202 (2009).